RESEARCH ARTICLE

ADVANCED
PHOTONICS
RESEARCH
Open Access

www.adpr-journal.com

Cladding-Free Antiresonance in Tubular Structures

Jiayu Zhao, Jiaao Yan, Zhanghua Dong, Chang Liu, Yongpeng Han, Yan Peng,*
Wei Lin,* and Yiming Zhu*

Antiresonance reflection (ARR) effectively turns tubular structures into functional devices ranging from waveguides to spectrometers and sensors, thus attracting a growing number of interests in recent years. Yet, ARRs are generally enabled inside the designed tube cladding with certain structural properties, which essentially acts as a quasi-Fabry–Pérot (F–P) cavity. This limits the application of the ARR effect on popular tubular entities in non-F–P cladding morphology, such as the chiral helical material or the self-rolled-up ultrathin/meshy membrane. Here, the scheme of core-antiresonant reflection (core-ARR or CARR) based on the leaky F–P effect is proposed, which validates ARRs inside the central core rather than the cladding of hollow tubes, hence expanding the optional scope of materials and constructions for tubular substances. Briefly, the CARR behavior is demonstrated in cylindrical, polyhedral, spiral, meshy, and notched hollow tubes with either transparent or opaque cladding materials. More importantly, tubular structures with CARR modes can be flexibly tuned in terms of the resonant frequency, which is used herein for sensitive detection of the environmental pressure, humidity, and thermal influence. As the CARR effect promotes interactions between light and various tubular structures, it holds promise for future opportunities in fields of physics, biophotonics, and material science.

1. Introduction

Antiresonance reflection (ARR) is one of the crucial interactions between light and tubular structures,[1–5] which occurs during electromagnetic (EM) waves oscillation inside the Fabry–Pérot (F–P)-like cladding of hollow tubes, as shown in **Figure 1**a. Accordingly, resonantly optical components penetrate the cladding and leak out, while the nonresonant ones are guided along the central core, thus forming a broadband antiresonant transmission mode with periodically tunable spectral dips

(as resonant frequencies). Owing to this point, the ARR effect enables plenty of splendid applications in fields of physics, biophotonics, and material science, such as low-loss waveguides from ultraviolet[1–3,5] to terahertz (THz)[6] bands, optofluidic chips for gas/liquid atomic spectroscopy,[7–11] and multifunction sensors for biochemical samples[12,13] or physical parameters[4,14] like displacement, strain, pressure and temperature, etc.

In these efforts, fundamental connections have been built between ARRs and the artificial tube's cladding, whose structural morphology might be either simple or complex, as displayed in Figure 1b, but necessarily acting as a quasi-F–P cavity. However, this essential cladding condition hinders many other tubular structures (Figure 1c) from being ARR-type optical resonators. For example, as for the currently popular helical materials, such as chiral ceramics[15] and elastic metal springs,[16] their spiral walls can obviously not play the role of an equivalent F–P unit and so does a multihole tube with the mesh-structured cladding.[17–19] Moreover, as for the self-rolled-up 2D material,[20,21] the cladding is usually too thin for internal oscillations and resonances of the interested EM bands. In view of the earlier facts, resolving this ARR capability could provide more tubular materials with a new perspective on strengthening the interactions with light and extending related applications.

Instead of routinely studying the cladding, we focused on the commonality of hollow core for various tubular structures (Figure 1b,c), which itself is a curved leaky F–P cavity and thus

J. Zhao, J. Yan, Z. Dong, Y. Han, Y. Peng, Y. Zhu
Terahertz Technology Innovation Research Institute
Terahertz Spectrum and Imaging Technology Cooperative Innovation Center
Shanghai Key Lab of Modern Optical System
University of Shanghai for Science and Technology
Shanghai 200093, China
E-mail: py@usst.edu.cn; ymzhu@usst.edu.cn

The ORCID identification number(s) for the author(s) of this article can be found under https://doi.org/10.1002/adpr.202200148.

C. Liu
Shanghai Institute of Optics and Fine Mechanics
Chinese Academy of Sciences
Shanghai 201800, China

Y. Peng, Y. Zhu
Shanghai Institute of Intelligent Science and Technology
Tongji University
Shanghai 200092, China

W. Lin
Institute of Modern Optics
Nankai University
Tianjin 300350, China
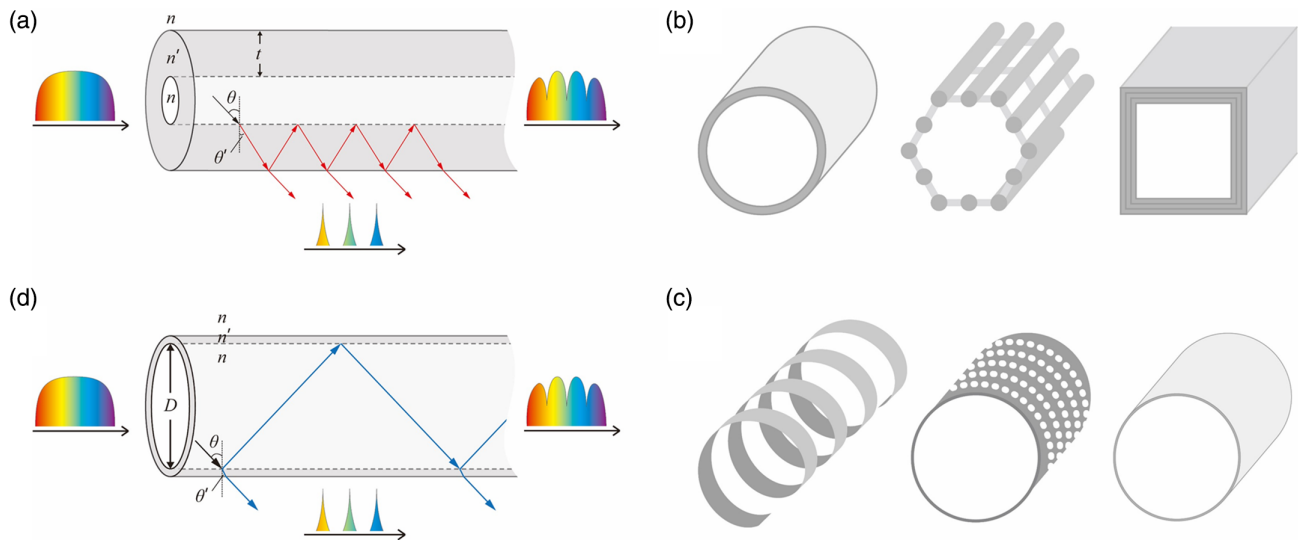E-mail: 019006@nankai.edu.cn

Figure 1. ARR and tubular structures. a) A typical ARR structure with F–P-type optical oscillations in the cladding. b) Several representative ARR tubes, including a cylindrical pipe,[6] a hexagonal cage,[7,8] a quadrilateral multi-layer channel,[9–11] and a ring-nested fiber.[1] c) Several representative tubes inside which the traditional ARR effect cannot work, including a helix,[15,16] a multihole tube,[17–19] an ultra-thin tube[20,21] and a thick-walled hole.[30] d) The suggested core-anti-resonant reflection (core-ARR or CARR) theory is considered within the central core of the tube.

theoretically allows ARRs of an input Gaussian beam between the cladding–core interfaces, as shown in Figure 1d. More detailed deductions are given in Section SA, Supporting Information. We named this scheme (after the traditional ARR) as the core-antiresonant reflection (core-ARR or CARR), whose unique feature is expected to be less dependent on the cladding's materials and constructions, thus offering possibilities for expanding the antiresonance effect to more tubular materials like those in Figure 1c.

In order to investigate the proposed CARR nature, comprehensive experiments were carried out in this work by adopting diverse tubular structures, including cylindrical, polyhedral, spiral, meshy, and notched hollow tubes with either transparent or opaque cladding materials, as well as a thick-walled hole. It has been demonstrated that the above tubular entities indeed become CARR-type resonators, which were then used for sensing the ambient pressure, heat, and humidity with high sensitivities. Hence, the CARR principle has provided a new degree of freedom toward light tuning by tubular cavities (a brief summary in Section B, Supporting Information). It is also worth mentioning that, although we proved the theory with millimeters–diameter tubes and THz waves, the presented CARR technique is promising to be generalized to tubular structures in other sizes using light sources with proper wavelengths after carefully considering the scaling law.

2. Verification of the CARR Theory

To begin with, we chose the most common A4 paper to produce CARR tubes. The craft processes are displayed in **Figure 2**a by two means and detailed descriptions are in Section C, Supporting Information. Briefly, we rolled a hollow cylinder with a single-layer paper cladding, whose inner diameter (D), cladding thickness (t), and length (L) were easily hand-made into around

10, 0.08 mm (i.e., paper thickness), and 15 cm. $D = 10$ mm is brought into the well-known F–P Equation

$$f_m = mc/(2nD\cos\theta) \tag{1}$$

where f_m is the resonant frequency, $m = 1, 2, 3...$ is the resonance order, c is the speed of light in vacuum, n is the refractive index between two reflecting interfaces with separation of D, and θ is the incident angle of light on the interface, as shown in Figure 1d. By further considering the grazing incidence of light waves into the tube and temporarily setting $\theta = 85°$, the resonant frequencies f_m can be calculated as 0.17, 0.34, 0.52 THz ... that is, in THz regime. Coincidentally, THz waves satisfy the studied CARR condition (Figure 1d), since it can both penetrate nonpolar materials (e.g., paper) and be partly reflected simultaneously due to the large θ. Hence, THz transmitter and detection modules were utilized in the following experiments, and the corresponding setup is drawn in Figure 2b as a conventional time-domain spectroscopy (TDS) system for measuring temporal waveforms of THz pulses (Section D, Supporting Information).

THz signals were collected in three different situations; as shown in Figure 2c (I), the transmitter and detection modules were arranged in a common focus for detecting the THz reference; (II) the paper tube was placed in the middle with two open ends coinciding with the two modules' foci; and (III) the tube was removed without any other changes. Accordingly, the transmitted THz spectra are shown in the same figure, which were retrieved by applying Fourier transformations (FT) on the experimentally recorded THz temporal waveforms. For case (I), the initial THz spectrum (black solid line) peaked at ≈0.4 THz and gradually decreased to the noise level beyond 1.4 THz. For case (II) with the paper tube, an intense THz spectral signal (red dashed line) was observed with five periodic peaks/dips as expected from Figure 1d. For case (III), the THz signal strongly
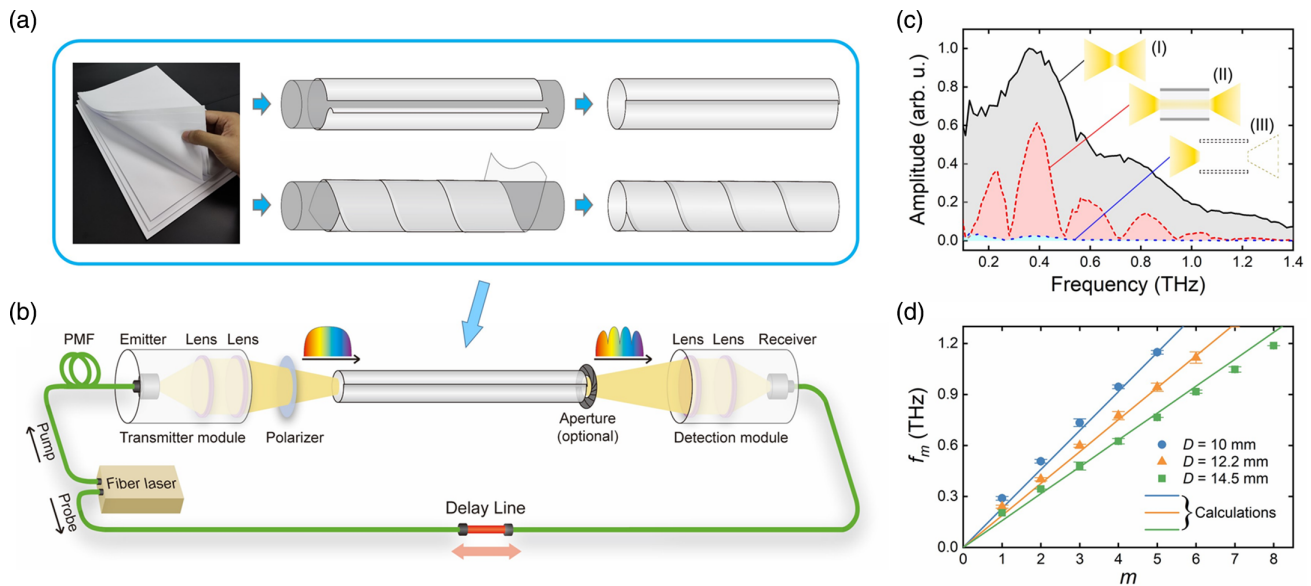
Figure 2. Demonstration of the CARR theory. a) Simple methods to make cylindrical tubes by paper. b) The paper tube was tested in a typical THz TDS system. c) The detected THz spectra, including the initial signal (I), and the transmitted signals along the paper tube (II) or after the free-space propagation (III). d) The resonant frequency f_m [spectral dips in (c)] as a function of its order m for three different inner diameters D of the paper tubes, with fitting lines given by Equation (1).

diffracted during the free-space propagation and became too little to be detected (blue dotted line).

In order to reconfirm the observed phenomena, we tested paper tubes with three different D values (10, 12.2, and 14.5 mm), and their spectral dips are quantified and plotted in Figure 2d as circles, triangles and squares, respectively. In the same figure, three solid lines represent the calculated results according to Equation (1). Best fittings were achieved at $\theta = 86.3°$, which is closed to the experimental value by tracing the THz beam around the focus (not shown). Till now, the theory of CARR has been primarily demonstrated.

Notice that, only the CARR effect dominates in the above paper tube experiments. Actually, the coexistence of cladding-ARRs and core-ARRs (CARR) can also be observed inside one pipe if the cladding thickness is increased to be several times larger than the wavelength of THz waves. Here we measured five PVC tubes with $D \approx 10$ mm, $L \approx 15$ cm, and wall thickness t ranging from 0.6 to 1 mm in step of 0.1 mm. By carefully checking the first antiresonant window (0–0.3 THz) of the five tubes as shown in the left part of **Figure 3**a, shifts of tiny dips (pointed by blue arrows) were discovered as a function of t. This relationship was further quantified as solid squares on
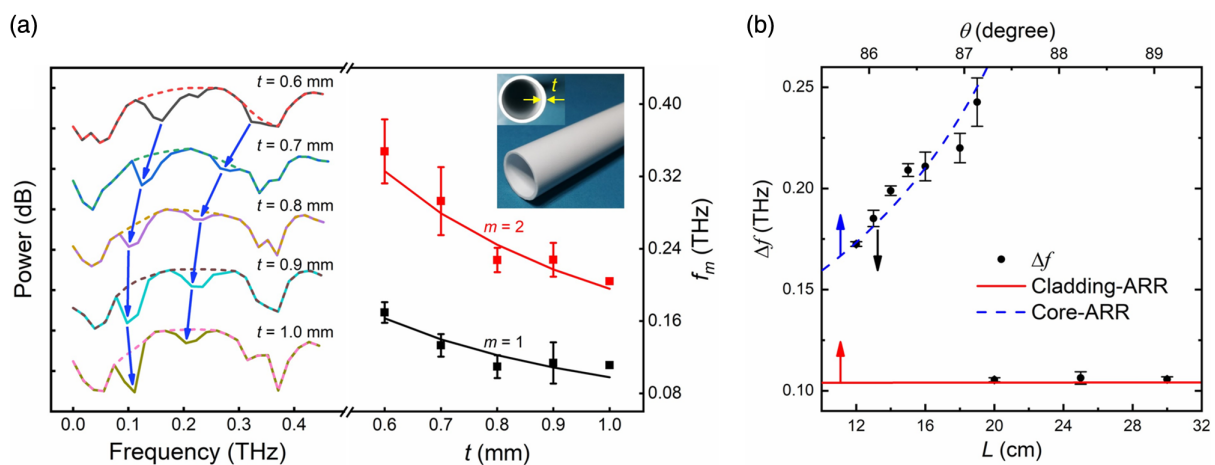

Figure 3. Coexistences of cladding-ARRs and CARR. a) Left: the transmission spectra of cylindrical PVC tubes with different wall thicknesses t. Spectral dips f_m ($m = 1$ and 2) pointed by blue arrows were caused by the cladding-ARR effect. Right: f_m decreased with the increasing t, in agreement with the theoretical predictions (solid lines) given by Equation (2). b) Variation of Δf (circles) with respect to the PVC tube length (L), indicating the conversion from core-ARR-to cladding-ARR-propagation modes. Blue and red fitting lines are calculated by Equation (1) and (2), respectively, considering the relationship between Δf and θ.

the right side of the same figure, along with fittings (solid lines) computed by Equation (2), which is in fact Equation (1) with n, D, and θ replaced by n' (= 1.83 for cladding index in THz band), t, and θ'

$$f_m = mc/(2n't\cos\theta') \qquad (2)$$

Furthermore, we also varied the length L (from 12 to 30 cm) of a PVC pipe in D of 12 mm and t of 1 mm, and the resultant Δf as the mean interval between major resonant frequencies are shown as circles in Figure 3b as a function of L. It can be observed that before $L = 20$ cm, Δf gradually increased and was well fitted by the blue dashed line given by the Δf–θ relation in Equation (1). This phenomenon can be attributed to core-ARRs of the THz beam with an increasing θ during propagation along the tube. In contrast after $L = 20$ cm, Δf decreased rapidly and became unchanged, which agrees with the cladding-ARR prediction computed by Equation (2) as the red solid line.

The above evolution from $\Delta f_{\text{core}-\text{ARR}}$ to $\Delta f_{\text{cladding-ARR}}$ hints that the core-ARR effect dominates in short tubes and will be completely converted into stable cladding-ARR modes in long-range waveguides. For this reason, in the following sections, we worked on short tubular structures (mostly in L of 15 cm), and concentrated on the filtered resonant frequency due to the CARR effect (in Section 3) and corresponding tuning and sensing applications (in Section 4), rather than focusing on its transmission mode and energy loss (related investigations are provided in the Section E and F, Supporting Information, and numerical simulations).

3. Cladding-Free CARR Mechanism

Based on the CARR technique, one has a wide range of choices on materials and structures of the tube cladding. Aiming at verifying this point, we tested various tubular entities as shown in **Figure 4** and **5**, revealing the versatility of the CARR theory.

3.1. Cladding Materials

In Figure 4a, nonpolar materials in the THz band with low material loss were rolled into single-layer tubes in D of about 12 mm and L of 15 cm, including the plain A4 paper (in thickness of ≈0.08 mm), the coated paper from magazines (0.054 and 0.17 mm), the sandpaper (0.25 mm), and the PVC plastic (0.05, 0.2, and 1 mm). Beside each tube picture, the output THz spectra are presented with vertical offset for clarity. Clear resonant frequencies are highlighted by gray dashed lines. Furthermore, as shown at the bottom, a paper helix was also made (Section C, Supporting Information) with a paper tape in the width of 5 mm and the helical pitch could be between 1 and 5 mm. Surprisingly, the resultant THz spectrum is still in good agreement with the above ones, validating the CARR effect on this important spiral structure.

In contrast for a tube made of polar materials in THz band (e.g., metal film), as its cladding is opaque for THz waves which contradicts the CARR condition (Figure 1d), thus the CARR effect (periodic spectral dips) cannot be observed. This hypothesis is confirmed by the first signal in Figure 4b achieved with a tin-walled tube whose geometric parameters were similar with the tubes in Figure 4a. However, the absent CARR nature can be easily regained by enhancing the light transmission through the tube cladding, for example, via porous/multihole structures or helical air clearances on the cladding wall. Note that these appearances are frequently found on either natural or artificial tubular structures, as shown in Section G, Supporting Information.

We first tried a simple method by adding a longitudinal slot in width of about 2.5 mm on the tin wall of the tube to increase the
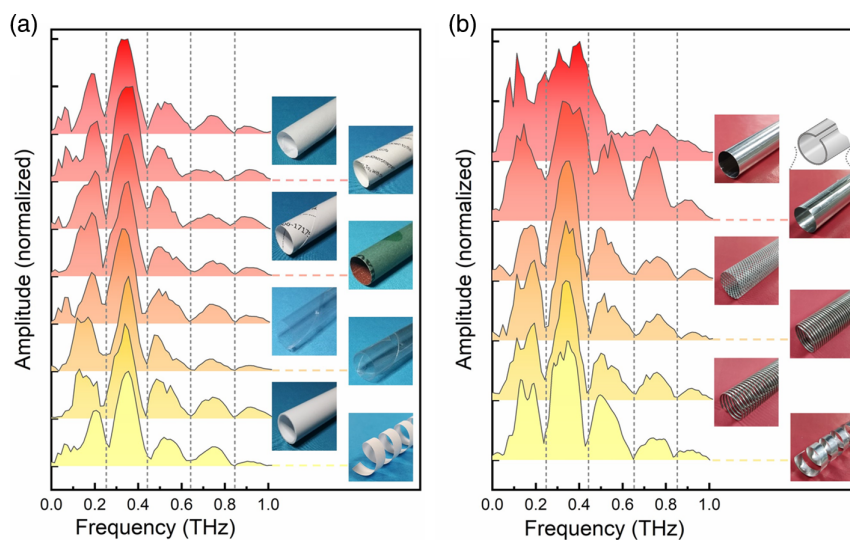

Figure 4. Diversity of the CARR cladding materials. a) Normalized transmission spectra (left) through tubes (right) made of different nonpolar materials with high transparency in THz band, namely, A4 paper, coated paper from magazines, sandpaper, thin plastic, and paper spring, respectively. b) Similar spectra with (a) except for the cladding made by polar materials instead. From top to bottom, the insets show a single-layer tinfoil tube, the same tin tube with a longitudinal slot covered by transparent tapes, an aluminum-wire meshy tube, two stainless steel springs with different pitches, and a tinfoil helix, respectively.
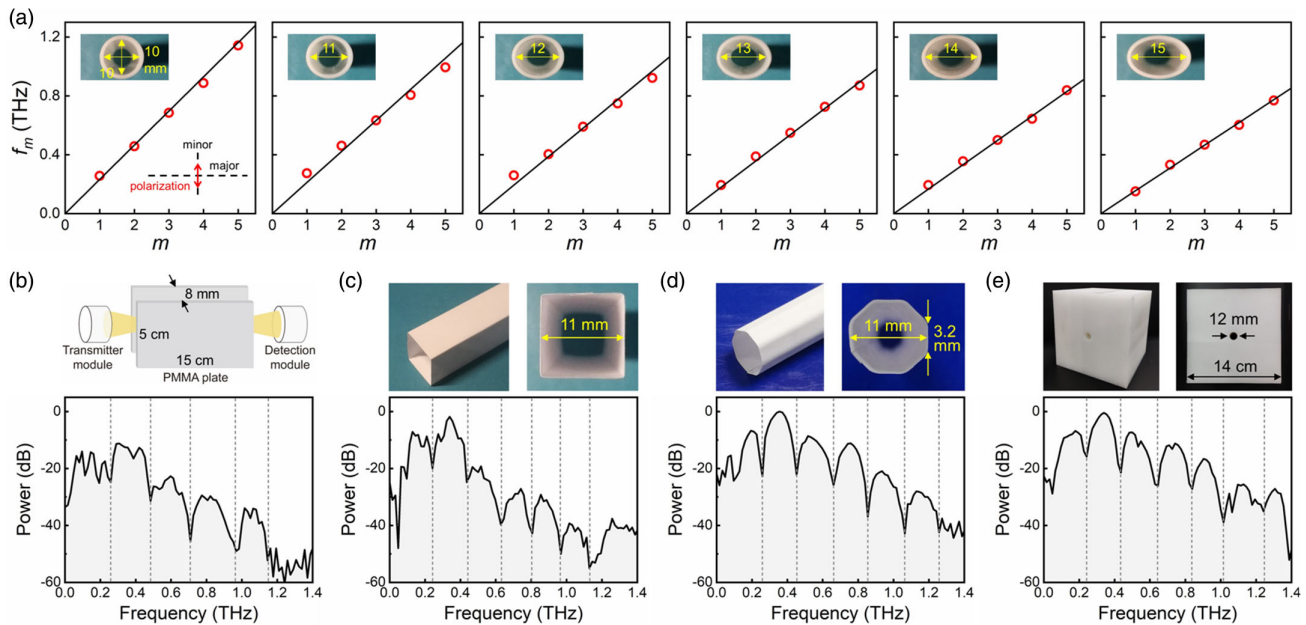
**ADVANCED
SCIENCE NEWS**

www.advancedsciencenews.com

**ADVANCED
PHOTONICS
RESEARCH**
Open Access

www.adpr-journal.com

Figure 5. Flexibility of the CARR tube morphology. a) The output f_m (open circles) evolution from tubes with different transverse sizes. Solid lines were obtained by substituting the major axis length of the tube's cross section for D in Equation (1). The incident THz waves was polarized along the minor axis. b–e) The parallel plates, quadrilateral and octagonal paper tubes, and the hollow air hole with large wall thickness (upper) and the corresponding CARR spectra (lower).

local THz transmission, and then we covered the slot with a transparent tape to maintain THz reflections at the same time. As indicated in Figure 4b, now the spectral signal was restored with periodical dips (i.e., resonant frequencies), which might be further optimized by modulating the slot geometry. Subsequently, we worked on an aluminum mesh tube with square holes in size of 1×1 mm and two stainless steel springs with wire diameter of 0.8 mm and pitches of 0.33 and 0.68 mm, respectively. Their spectra were more like the ones in Figure 4a owing to sufficient THz penetrations through the cladding.

Furthermore, we have also tested helical tubes rolled up by a tin tape and detected the expected CARR effect (at the bottom of Figure 4b). Till now, both dielectric and metal spiral structures have found an unprecedented access to antiresonantly interact with light modes, which might pave the way toward interdisciplinary applications based on, for example, chiral inorganic materials,[15] metal springs,[16] carbon coils[22] and helical proteins/DNA,[23–25] etc.

3.2. Cladding Morphologies

Besides the wide range of available cladding materials proved earlier, another impressive characteristic of the CARR resonator is the flexibility of cladding constructions, which can be not only cylindrical or helical tubes, but also elliptical or polyhedral structures, as well as a bare hole, as shown in Figure 5.

Firstly, six 3D-printed PVC plastic tubes (in length of 15 cm) with quasielliptical cross sections (in thickness of 1 mm) were successively tested as shown in Figure 5a. Specifically, the major axis length (defined as D') of the ellipse was enhanced from 10 to 15 mm, while the minor axis length (D'') was fixed at 10 mm.

Then, the THz polarizer in our experimental setup (see Figure 2b) was adjusted so that the THz wave polarization was along the minor axis before entering the elliptical tubes. The output THz resonance frequencies f_m were obtained as open circles in Figure 5a. Obviously, the overall f_m decreased with the increasing D'. Since here D' is the only variable, it was adopted to substitute for D in Equation (1), and the calculation results are drawn as solid lines, fitting the experimental data. This agreement actually reveals that the transverse-electric (TE) polarized THz wave plays the leading role in CARR tubes. This polarization dependence has also been reported in waveguides like parallel metal plates,[26,27] inside which the internal reflections of TE waves are stronger than that of the transverse-magnetic ones.

Taking the above TE polarization dependence into consideration, then, a pair of parallel plates was tested, as schematically drawn in Figure 5b, which was made of polymethyl methacrylate (PMMA) in thickness of 1 mm, width of 5 cm, length of 15 cm, and the separation distance was about 8 mm. Accordingly, the transmission spectrum is shown in the lower part of Figure 5b, in which the vertical dashed lines guide eyes to the resonant frequencies caused by the CARR effect. Moreover in Figure 5c,d, polyhedral tubes with quadrangular and octagonal cross sections were made by paper folding, whose inner diameters (distance between two opposite sides) and length were both around 11 mm and 15 cm. On corresponding THz transmission spectra, CARR phenomena can still be clearly observed. Finally in Figure 5e, a 12 mm-diameter air hole centered inside bulk polyethylene (PE) of length 15 cm was experimented with and the resultant THz spectrum showed CARR behavior. All these evidences in this section strongly revealed the structural diversity of tubular cavities given by the suggested CARR mechanism.

Moreover, slight bending of CARR structures would not break the antiresonance results, as shown in Section H, Supporting Information.

4. Applied Examples Based on CARR Structures

The above sections have convinced that various tubular structures do make CARR-type resonators, whose resonant frequency f_m can be theoretically tuned by the tube parameters, that is, the inner diameter D or refractive index n as written in Equation (1). On the other hand, if any external influence on the tube (as factor X) could change its D or n, then the correlation of f_m−X would promise interesting sensing cases. For instance, natural or artificial tubular structures (such as biological specimens or spiral materials) might serve as optical resonators/sensors toward

diverse ambient conditions, like the gas pressure, the fluidic refractivity, and the temperature or humidity change, etc. In this section, we set three simple examples by studying the spectral response of hand-made CARR tubes to the external stress, heat, and humidification effects.

4.1. The Pressure Sensor

Six tubes with characteristic designs were divided into two groups and tested successively, as shown in **Figure 6**. First, an ordinary paper tube in length of 15 cm was forced on both sides (pointed by blue arrows), as indicated in Figure 6aI, whose cross section was then compressed into an elliptical-like shape with long and short axes, and the incident THz polarization was adjusted along the latter (dashed line). The monitored THz spectral outputs are shown in the inset of Figure 6b, in which the
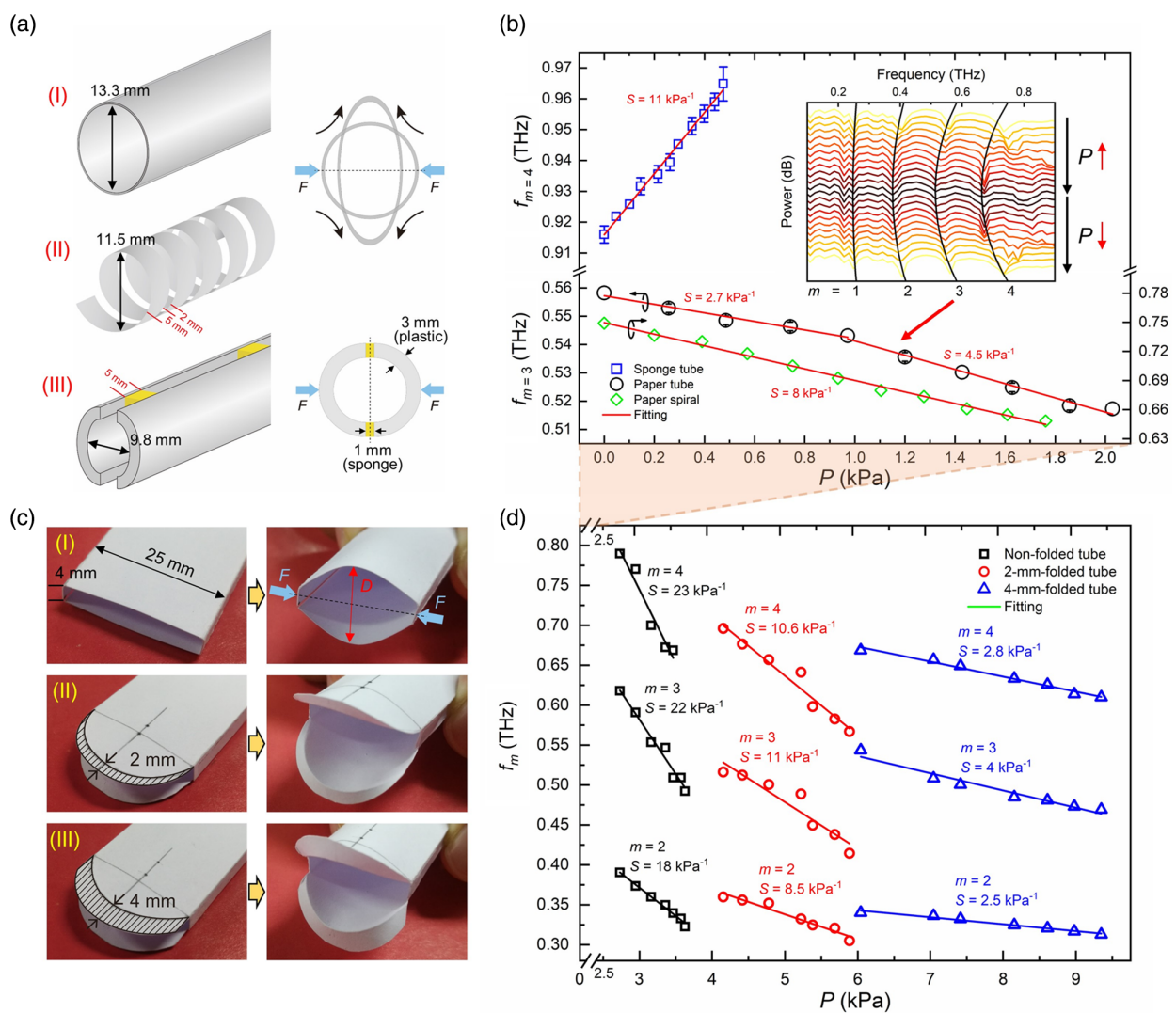

Figure 6. A CARR-type application on sensing the ambient stress. a,c) The used six CARR tubes with different sensitivities S and pressure P ranges. The tube claddings were made using different materials (paper, sponge) or morphologies (cylindrical, helical, and quadrilateral) or structural modulations (folded-up ends in width of 2 and 4 mm). The input THz polarization direction was along the dashed lines, while the ambient force was applied as pointed by blue arrows with the letter of "F". b,d) The correlations between resonant frequencies f_m and the applied P for the above tubes. The inset in (b) illustrates the f_m shifts during the growth and decline of P on the first paper tube in (a).

upper and lower halves correspond to first increasing and then decreasing the applied pressure P, respectively. Also in the inset, vertical black curves highlight the shift of f_m at different m, which could be calibrated as follows. Setting $m = 3$ as an example, the relationship between $f_{m=3}$ and P is extracted from the inset and presented in Figure 6b as black circles. By piecewise linear fittings (red lines), the quantitative connections have been built between the external pressure and the CARR spectral response, in which way a basic paper tube acted as a stress sensor. Moreover, the sensing sensitivity can be evaluated by the S parameter defined by $S = |\Delta(\Delta f / f_0)/\delta P|$,[28] where f_0 is the resonance frequency without external loads, and Δf is the variation of f_0 under a certain pressure P. The calculated results are $S \approx 2.7 \ \mathrm{kPa}^{-1}$ below $P = 1 \ \mathrm{kPa}$, and $S \approx 4.5 \ \mathrm{kPa}^{-1}$ in the range of $1 \ \mathrm{kPa} < P < 2 \ \mathrm{kPa}$.

The above S values can be further enhanced either by modifying the structure of the original paper cladding or using more elastic cladding materials. Based on the former thought, we cut the cylindrical paper cladding into a helix, as shown in

Figure 6aII, and then repeated the same experiment. The measured $f_{m=3}$–P relationship is indicated in Figure 6b as green diamonds, leading to an enhanced $S = 8 \ \mathrm{kPa}^{-1}$. While for the latter thought, we changed the paper cladding into a combination of two half plastic tubes (3 mm thickness) and four sponge spacers (in yellow, 3 mm × 1 mm × 5 mm), as shown in Figure 6aIII. Via this configuration, the elastic sponge could absorb the external pressures and its initial 1 mm thickness (as well as the inner diameter of the tube) would decrease with the increasing P. Meanwhile, the input THz polarization was orthogonal to the P direction (black dashed line vs. blue arrows). Then, the stress test was carried out again and the resultant $f_{m=4}$–P is plotted in the upper part of Figure 6b as blue squares. Compared with the previous paper tubes, now the sensitivity S has been improved up to $\approx 11 \ \mathrm{kPa}^{-1}$, which is a competitive value with pressure sensors based on hydrogel as reported in the study by Lu et al.[28]

Beyond the above cylindrical or spiral style, CARR sensors can also be flexibly designed in order to meet the demand of an extended P range while maintaining high S values. For this
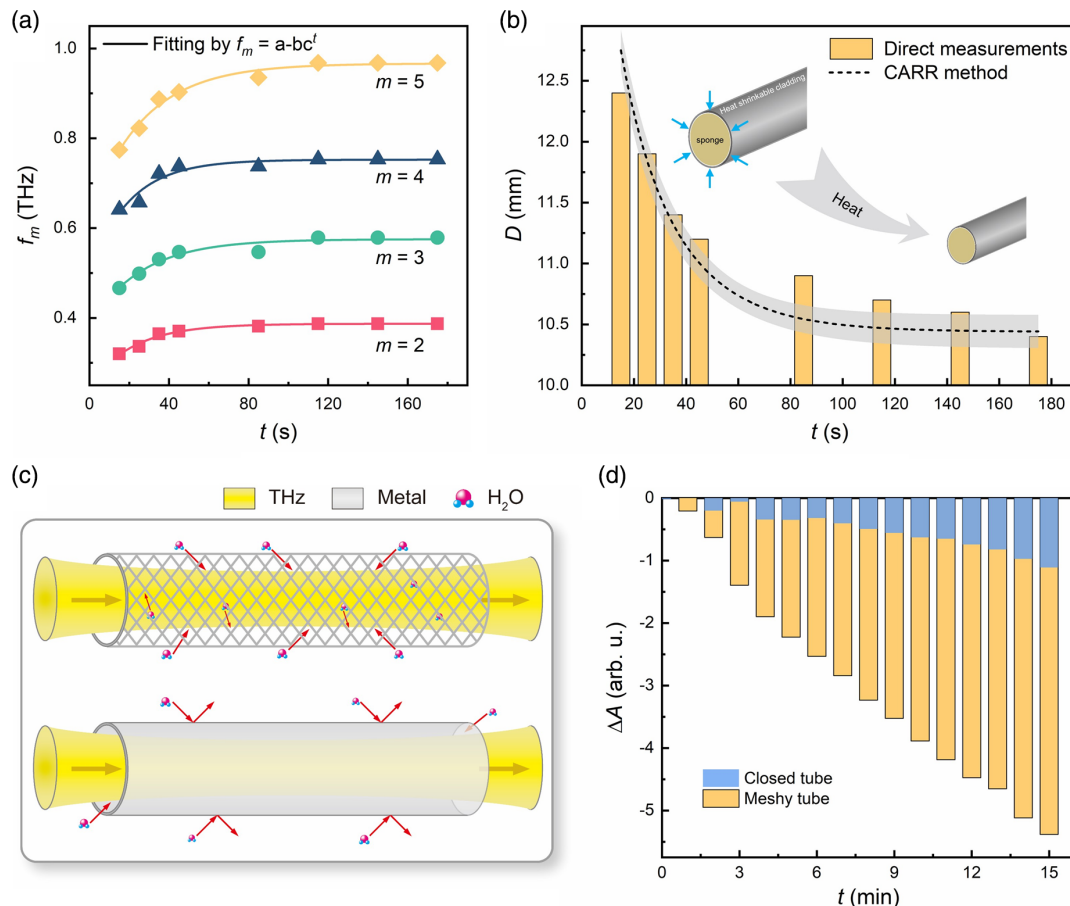

Figure 7. CARR applications on response to the ambient heat and humidity. a,b) The CARR tube played the role of a reactor to the environmental thermal effect. a) f_m increased with time t in case of heating a heat-shrinkable tube whose diameter D gradually decreased. b) The black dashed line and the accompanying gray area (error zone) represent the retrieved D from the fitting curves in (a) via Equation (1), and the yellow bars indicate the directly measured results. c, d) The CARR tube acted as a light cage for interactions between THz waves and the incoming water vapor. c) The schematic diagram of the sealed chamber, inside which a meshy CARR tube and a closed tin tube were set. The injected water vapor was more easily captured by the CARR tube due to its meshy cladding. d) Both THz spectral amplitudes of the two tubes decreased after being absorbed by water molecules. However, this THz–water interaction process is accelerated by the CARR cage.

**ADVANCED
SCIENCE NEWS**
www.advancedsciencenews.com

**ADVANCED
PHOTONICS
RESEARCH**
Open Access
www.adpr-journal.com

purpose, we made a quadrilateral paper tube in length of 15 cm whose cross section was a rectangle in size of 25 mm × 4 mm, as shown in Figure 6cI. The experimental processes on this tube were similar to that in Figure 6a. The transmitted THz spectra and the corresponding pressure values were recorded while the separation distance D (red double-headed arrow) between two long sides increased from 10 to 15 mm in step length of 0.5 mm. Three resonant frequencies f_m ($m = 2, 3,$ and 4) are extracted and plotted as functions of P in Figure 6d as black open squares, along with linear fittings. At present, not only the bearable P region has been enlarged to round 3 kPa, but also a larger $S = 23$ kPa^{-1} has been successfully achieved.

Next, we introduced the rectangular tube with two round edges on both ends, which were then folded up along the arc trajectories as shown in Figure 6cII, III (see also Section I, Supporting Information). This procedure borrowed the foldable nature of paper, providing a convenient way to modify the cladding properties via origami.[21] With the existence of folded edges on both ends, the cladding structure was strengthened with mechanical function, since right now the same change of the separation D required larger external pressure to conquer

the heavier edge bending (Video S1, Supporting Information). Thus the spectral response regions of the two edge-folded CARR tubes (with maximum arc width of 2–4 mm) were different from the rectangular one, as shown in Figure 6d within 2–4, 4–6 and 6–9.5 kPa, respectively. If further complemented by the cylindrical tube at 0–2 kPa in Figure 6b, totally four distributed $f_m−P$ areas have been formed, validating our pressure-sensing scheme based on the CARR effect. Meanwhile, all S values remained at a high level of more than 2 kPa^{-1}. Compared with publications[28,29] inside which the popular MXene-based materials were used for making pressure sensors, our sensitivities are competitive within our P range of about 0–10 kPa and we even achieve a maximum S value of 23 kPa^{-1}. However, in view of the larger pressure applied in the references, our P range should be further extended in future works, for example, by varying the tube cladding materials.

4.2. The Thermal Reactor

The above pressure-sensing experiment has set a typical instance for environmental monitoring via CARR tubes. On the other
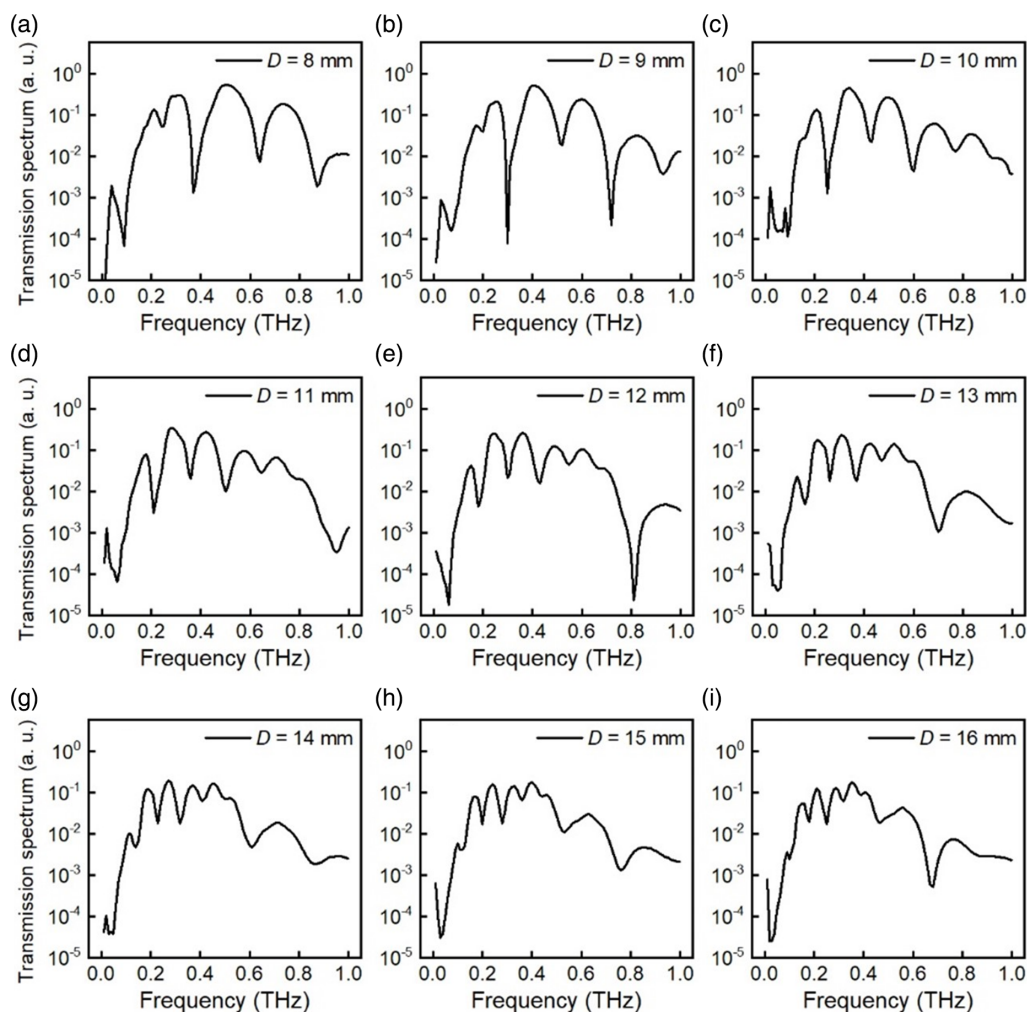

Figure 8. The simulated transmission spectra given by CARR tubes in different core diameters.

ADVANCED
SCIENCE NEWS

www.advancedsciencenews.com

ADVANCED
PHOTONICS
RESEARCH
Open Access

www.adpr-journal.com

hand, in a stable surrounding condition, the tube's property itself as a function of time might be the central concern. This happens in case of, for example, diagnosing the time-varying diameter of a tubular specimen of interest in biological systems.

Following this clue, we established such a CARR tube by rolling typical heat-shrinkable tube materials around a cylindrical sponge core in diameter of about 12.5 mm and length of 15 cm, which was then exposed to the ambient temperature set at 90 °C. While the tube interfaced with the surrounding heat, the diameter D was real time monitored by recording the transmitted THz spectra in time intervals of tens of seconds. The resultant f_m at $m = 2, 3, 4$, and 5 are plotted in **Figure 7**a as symbols with respect to the heat-up time t, whose gradual growth is induced by the decreasing D as expected. Colorful lines are the corresponding fittings given by the exponential relationship of $f_m = a - b \times c^t$, where a, b, and c are any constants. Next, the time-varying diameter of the CARR tube was determined by substituting the fitting values of f_m into Equation (1) and then solving the remaining D. Figure 7b displays the calculated D as the black dashed line within a gray area as the error margin. In the same figure, the vertical bars are the directly measured D by side images of the tube. It can be observed that the two evolutions of D values are in good agreement.

4.3. The Light Cage

Besides the above two cases benefiting from the geometrical (diameter) change of the tubular sensors, CARR tubes can also be adopted as static devices such as optofluidic channels or gas/liquid cells. In this aspect, we remind ourselves that the meshy metal tube in Figure 4b has an additional capability of efficiently capturing gas or liquid samples from surroundings via diffusion through the meshy cladding, as featured in the concept of light cages.[7,8,18] Hence, here we carried out an experimental comparison on THz spectral responses to the ambient water vapor, between the meshy CARR tube and the tin tube both ever used in Figure 4b.

As schematically shown in Figure 7c, the water vapor was slowly injected into a sealed chamber, inside which the two tubes were mounted and filled with paper scraps for trapping moisture. The decreasing amount (ΔA) of the transmitted THz amplitude at peak frequency was detected and plotted in Figure 7d as a function of time t for each tube. It can be clearly seen that the THz energy was absorbed by the vapors in both tubes, while the meshy CARR cage has an obviously more intense response to the humidity than the closed tin tube. This CARR advantage might help porous channels find applications like the integrated spectrometer for sampling the ambient gas/liquid atoms.
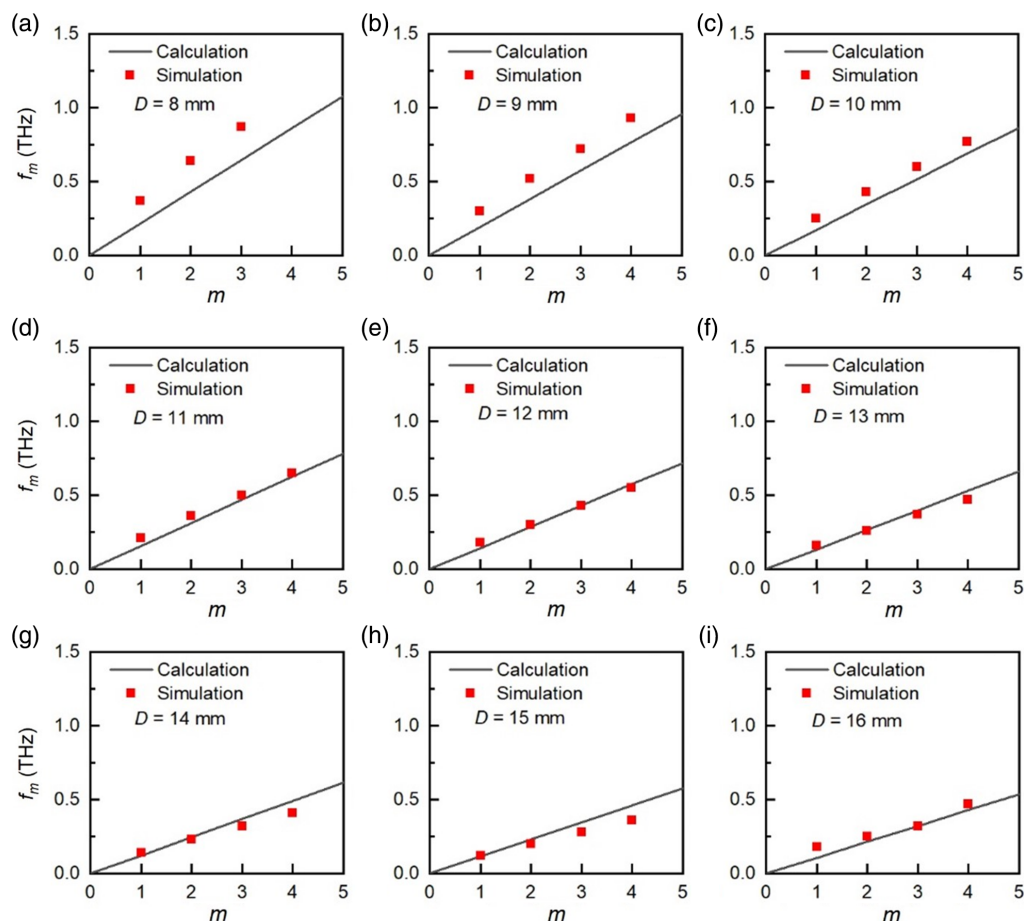

Figure 9. The simulated resonant frequencies (red squares) of CARR tubes in different core diameters (8–16 cm), along with fittings (black lines) calculated by Equation (1).
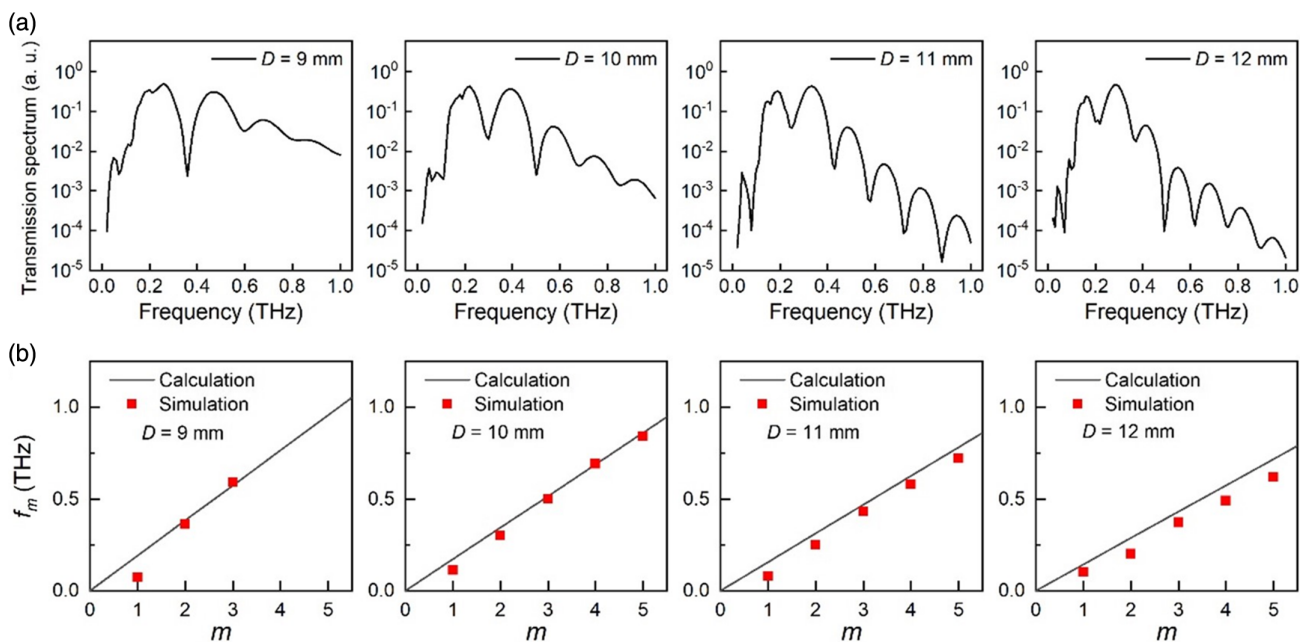
Figure 10. a) The simulated transmission spectra of the square paper tube with core diameter $D = 9$–12 mm. b) The resonant frequencies (red squares) obtained in (a), along with fittings (black lines) calculated by Equation (1).

5. Numerical Simulations

In order to examine the experimental CARR effect, numerical simulations have been performed by the commercial software Rsoft. Our parameters of $D = 8$–16 mm, $t = 0.08$ mm, and $n' = 1.6$, as well as $L = 15$ cm and $\theta = 85°$, were all taken into consideration during building the model. The simulated transmission spectra are shown in **Figure 8**, inside which periodic resonant frequencies (dips) can be clearly observed.

More importantly, these frequency locations can be well interpreted by Equation (1), as indicated in **Figure 9**, demonstrating its CARR-type origin. That is, the simulated resonant frequencies of CARR tubes with different core diameters are plotted in Figure 9 as red squares, and the black lines are given by Equation (1) with three parameters, that is, $n = 1$ (air), $D = 8$–16 cm, and $\theta = 85°$, which were also used in simulations. The resulted fittings are acceptable for most D cases.

Next, simulations on the square paper tube are additionally carried out. Specifically, the simulated parameters are $D = 9$–12 mm in step of 1 mm, $t = 0.08$ mm, $n' = 1.6$, $L = 15$ cm, and $\theta = 85°$. The simulated transmission spectra are shown in **Figure 10**a, in which periodic resonant frequencies (dips) can be clearly observed. Moreover, these resonant frequency locations can be fit by Equation (1), as demonstrated in Figure 10b.

6. Conclusion and Outlook

In summary, in this work we have demonstrated the CARR mechanism to be a competitive candidate within resonance patterns for investigating the interactions between light and diverse tubular cavities. Briefly, two characteristics have been brought by the CARR effect to tubular resonators, namely, the flexibility of cladding materials and constructions and the tunability of resonant frequencies. The combined action of these two features has led to practical applications as we displayed in the way of optical sensing toward the ambient stress, humidity, and thermal influences with high sensitivity. Consequently, the proposed CARR principle would become a necessary consideration not only for the fabrication of tubular devices in the macroscopic scale, but also for the diagnosis of microscopic tubes in the biophotonics world.

The future development of CARRs, on one hand, lies in potential improvements of the tube properties for higher sensing sensitivity. On the other hand, the CARR effect has opened new paths for ultrathin materials, such as 2D materials, nanomembranes, soft electronic materials, and origami/kirigami materials, to be incorporated for producing the cladding mirrors of optical cavities in polyhedral or cylindrical morphologies. By this means, effective couplings between the CARR type and other physical fields are likely achieved, resulting in multifunctional devices with better performances. We hold confidences on that the CARR theory is promising to pave the way for tubular structures toward both fundamental innovations and diverse applications. New discoveries may soon come into being after this report.

Supporting Information

Supporting Information is available from the Wiley Online Library or from the author.

**ADVANCED
SCIENCE NEWS**

www.advancedsciencenews.com

**ADVANCED
PHOTONICS
RESEARCH**
Open Access

www.adpr-journal.com

Conflict of Interest

The authors declare no conflict of interest.

Data Availability Statement

The data that support the findings of this study are available from the corresponding author upon reasonable request.

Keywords

antiresonances, claddings, cores, Fabry–Pérot cavities, tubular structures

[1] C. L. Wei, R. J. Weiblen, C. R. Menyuk, J. Hu, *Adv. Opt. Photon.* **2017**, *9*, 504.

[2] W. Ding, Y. Y. Wang, S. F. Gao, M. L. Wang, P. Wang, *IEEE J. Sel. Top. Quantum Electron.* **2020**, *26*, 1.

[3] F. Yu, J. C. Knight, *IEEE J. Sel. Top. Quantum Electron.* **2016**, *22*, 146.

[4] W. J. Ni, C. Y. Yang, Y. Y. Luo, R. Xia, P. Lu, D. J. J. Hu, S. Danto, P. P. Shum, L. Wei, *Photonics* **2021**, *8*, 128.

[5] W. Ding, Y. Y. Wang, S. F. Gao, Y. F. Hong, P. Wang, *Acta Phys. Sin.* **2018**, *67*, 124201.

[6] C. H. Lai, Y. C. Hsueh, H. W. Chen, Y. J. Huang, H. C. Chang, C. K. Sun, *Opt. Lett.* **2009**, *34*, 3457.

[7] F. Davidson-Marquis, J. Gargiulo, E. Gómez-López, B. Jang, T. Kroh, C. Müller, M. Ziegler, S. A. Maier, H. Kübler, M. A. Schmidt, O. Benson, *Light: Sci. Appl.* **2021**, *10*, 114.

[8] J. Kim, B. Jang, J. Gargiulo, J. Bürger, J. B. Zhao, S. Upendar, T. Weiss, S. A. Maier, M. A. Schmidt, *Anal. Chem.* **2021**, *93*, 752.

[9] W. G. Yang, D. B. Conkey, B. Wu, D. L. Yin, A. R. Hawkins, H. Schmidt, *Nat. Photonics* **2007**, *1*, 331.

[10] H. Schmidt, A. R. Hawkins, *Laser Photonics Rev.* **2010**, *4*, 720.

[11] B. Wu, J. F. Hulbert, E. J. Lunt, K. Hurd, A. R. Hawkins, H. Schmidt, *Nat. Photonics* **2010**, *4*, 776.

[12] M. N. Velasco-Garcia, *Semin. Cell Dev. Biol.* **2009**, *20*, 27.

[13] V. M. N. Passaro, F. Dell'Olio, B. Casamassima, F. D. Leonardis, *Sensors* **2007**, *7*, 508.

[14] K. Benaissa, A. Nathan, *Sens. Actuators, A* **1998**, *65*, 33.

[15] J. C. Fan, N. A. Kotov, *Adv. Mater.* **2020**, *32*, 1906738.

[16] W. M. Li, G. S. Huang, J. Wang, Y. Yu, X. J. Wu, X. G. Cui, Y. F. Mei, *Lab Chip* **2012**, *12*, 2322.

[17] Y. Q. Wang, Y. Wang, G. S. Huang, Y. Kong, C. Liu, Z. Zhao, K. B. Wu, Y. F. Mei, *Adv. Photonics Res.* **2021**, *2*, 2000163.

[18] R. Briche, A. Benamrouche, P. Cremillieu, P. Regreny, J. L. Leclercq, X. Letartre, A. Danescu, S. Callard, *APL Photonics* **2020**, *5*, 106106.

[19] P. Danescu, P. Regreny, J. Cremillieu, L. Leclercq, *Nanotechnology* **2018**, *29*, 285301.

[20] Z. A. Tian, L. N. Zhang, Y. F. Fang, B. R. Xu, S. W. Tang, N. Hu, Z. H. An, Z. Chen, Y. F. Mei, *Adv. Mater.* **2017**, *29*, 1604572.

[21] Z. Y. Zhang, Z. A. Tian, Y. F. Mei, Z. F. Di, *Mater. Sci. and Eng. R* **2021**, *145*, 100621.

[22] Y. Qin, Y. Kim, L. B. Zhang, S. Lee, R. B. Yang, A. L. Pan, K. Mathwig, M. Alexe, U. Gösele, M. Knez, *Small* **2010**, *6*, 910.

[23] Y. Q. Zhou, M. Karplus, *Nature* **1999**, *401*, 400.

[24] S. O. Kelley, J. K. Barton, *Science* **1999**, *283*, 375.

[25] A. J. Wang, G. J. Quigley, F. J. Kolpak, G. van der Marel, J. H. van Boom, A. Rich, *Science* **1981**, *211*, 171.

[26] R. Mendis, D. M. Mittleman, *J. Opt. Soc. Am. B* **2009**, *26*, A6.

[27] R. Mendis, D. M. Mittleman, *Opt. Express* **2009**, *17*, 14839.

[28] Y. Lu, X. Y. Qu, W. Zhao, Y. F. Ren, W. L. Si, W. J. Wang, Q. Wang, W. Huang, X. C. Dong, *Research* **2020**, *2020*, 2038560.

[29] Y. Guo, M. J. Zhong, Z. W. Fang, P. B. Wan, G. H. Yu, *Nano Lett.* **2019**, *19*, 1143.

[30] L. A. Hof, J. A. Ziki, *Micromachines* **2017**, *8*, 53.